TU Delft

Delft University of Technology

# Tire dependence for the aerodynamics of yawed bicycle wheels

Jux, Constantin; Sciacchitano, Andrea; Scarano, Fulvio

**DOI**
10.1016/j.jweia.2022.105294

**Publication date**
2023

**Document Version**
Final published version

**Published in**
Journal of Wind Engineering and Industrial Aerodynamics

**Citation (APA)**
Jux, C., Sciacchitano, A., & Scarano, F. (2023). Tire dependence for the aerodynamics of yawed bicycle wheels. *Journal of Wind Engineering and Industrial Aerodynamics*, *233*, Article 105294. https://doi.org/10.1016/j.jweia.2022.105294

**Important note**
To cite this publication, please use the final published version (if applicable).
Please check the document version above.

**Copyright**
Other than for strictly personal use, it is not permitted to download, forward or distribute the text or part of it, without the consent of the author(s) and/or copyright holder(s), unless the work is under an open content license such as Creative Commons.

**Takedown policy**
Please contact us and provide details if you believe this document breaches copyrights.
We will remove access to the work immediately and investigate your claim.

*This work is downloaded from Delft University of Technology.*
*For technical reasons the number of authors shown on this cover page is limited to a maximum of 10.*

Journal of Wind Engineering & Industrial Aerodynamics 233 (2023) 105294

Contents lists available at ScienceDirect

Journal of Wind Engineering & Industrial Aerodynamics

journal homepage: www.elsevier.com/locate/jweia

# Tire dependence for the aerodynamics of yawed bicycle wheels

Constantin Jux, Andrea Sciacchitano *, Fulvio Scarano

*Faculty of Aerospace Engineering, Delft University of Technology, the Netherlands*

ARTICLE INFO

*Keywords:*
Cycling wheel aerodynamics
Particle image velocimetry
Sail effect
Drag minimization

ABSTRACT

The aerodynamic characteristics of a modern road cycling wheel in cross wind are studied through force- and planar PIV measurements in the TU Delft Open Jet Facility. The performance of the 62 mm deep rim is evaluated for three tire profiles, and yaw angles up to 24°. All measurements are executed at 12.5 m/s (45 km/h) free-stream- and wheel-rotational velocity. The wheel's rim-tire section in crosswind is found to behave similar to an airfoil at incidence, ultimately resulting in a reduction of the wheel's aerodynamic resistance with increasing yaw angle magnitude. This phenomenon, also referred to as the sail-effect, is limited by the stall angle of the tire-rim profile. The stall angle is found to depend critically on the tire's surface structure. Larger stall angles, resulting in lower resistance, are obtained if the tire profile triggers laminar-to-turbulent boundary layer transition.

## 1. Introduction

Aerodynamic drag is the major resistance a cyclist needs to overcome at speeds of 40 km/h and beyond. In fact, on level terrain and in absence of strong tail wind, the aerodynamic drag can account for approximately 90% of a rider's total resistance in this speed regime which is typical for road racing (Kyle and Burke, 1984). The wheels contribute to about 10% of the total aerodynamic drag (Greenwell et al., 1995), making them a crucial element in any cycling-performance optimization.

Focusing on road cycling, a rider is exposed to a variety of wind conditions, affecting the perceived yaw angle. The concept of wind-averaged drag (WAD, Ingram, 1978; Cooper, 2003) accounts for the statistically anticipated yaw-angle distribution experienced by a ground vehicle. The higher the vehicle velocity, the smaller the maximum yaw angle perceived for a given wind speed. For professional road cycling speeds, the probability of exceeding 20° yaw angle is reported to be less than 10% (Brownlie et al., 2010; Barry, 2018). Vice versa, a rider spends 90% of the time at yaw angles below 20°.

Aerodynamically designed wheels used in road racing (thus, excluding time-trial and triathlon specific multi-spoke and disc wheels) are characterized by a 40–80 mm deep rim section, that connects via a multitude of thin spokes to a cylindrical hub. In comparison to classical, shallow rim profiles, the deep-section rim increases structural stiffness and additionally fulfils two aerodynamic functions: on one hand, it streamlines the tire shape, effectively reducing the tire-rim drag coefficient. On the other hand, it generates —similar to a sail or airfoil— a side force perpendicular to the relative wind direction. A component of this force points in the riding direction, effectively "pulling" the wheel forwards and thereby further reducing its resistance in the direction of motion. The latter effect is known as the sail-effect in literature, and it can result in a negative net drag force for wheels at high yaw angles (Lukes et al., 2005; Barry et al., 2012; Malizia and Blocken, 2020a).

Designing a wheel for optimal performance is, however, not solely about minimizing (wind-averaged) drag. As Barry et al. (2012) point out, large lateral forces on a wheel yield strong steering moments and can be a concern of maneuverability. Similar concerns can be expressed when discussing the stall behavior for wheels at large yaw angles.

In addition to the rim-geometry, the aerodynamic characteristics of a wheel depend on the interaction of rim and tire. Crane and Morton (2018) investigate this interaction with specific attention to tire width relative to the rim. While focusing on tire width, Crane and Morton (2018) already speculate that "leading edge geometry", i.e. tire geometry, alters the stall angle of a given wheel. The hypothesis is supported by data from wheel manufacturers, claiming that the tire's surface texture conditions the boundary layer development for the flow over the wheel, and that forcing laminar-to-turbulent boundary layer transition on the tire is essential for drag minimization of bicycle wheels at large yaw angles (Cant, 2014).

To test the above hypothesis, this work presents wind tunnel force and velocimetry measurements on a state-of-the-art bicycle wheel, comparing its aerodynamic characteristics when fitted with (i) a regular, lightly textured tire; (ii) a smooth tire; and (iii) a smooth tire with a

* Corresponding author.
*E-mail address:* a.sciacchitano@tudelft.nl (A. Sciacchitano).

https://doi.org/10.1016/j.jweia.2022.105294
Received 17 February 2022; Received in revised form 1 December 2022; Accepted 24 December 2022
Available online 18 January 2023
0167-6105/© 2023 The Authors. Published by Elsevier Ltd. This is an open access article under the CC BY license (http://creativecommons.org/licenses/by/4.0/).

tripping element on its tread.

In the discussion of cycling wheel aerodynamics it is common practice to study wheels in isolation. Experimental studies in the field focus predominantly on balance measurements (e.g. Zdravkovich, 1992; Greenwell et al., 1995; Tew and Sayers, 1999), whereas flow topology data remains undocumented to the best of the authors' knowledge. Such data is readily available from computational fluid dynamics (CFD) analysis, which presents an active line of research in the context of cycling wheel aerodynamics (Godo et al., 2010; Malizia et al., 2019; Malizia and Blocken, 2020b). Authors developing numerical tools for the aerodynamic analysis of cycling wheels, however, have to rely on the experimentally documented force data for validation of their simulations. This practice becomes problematic when reported drag measurements for the same wheel show variations approaching up to 300%, as observed by Godo et al. (2010). The large force sensitivity is ascribed to variations in the experimental setup, including tire choice, free-stream turbulence, wheel support design and wind tunnel blockage.

In view of the gaps and discrepancies in literature, the present work provides an experimental analysis of the flow topology on a state-of-the-art bicycle wheel in crosswind and its dependence on tire surface properties. The change in flow topology with yaw angle and tire selection is documented. The acquired data is subsequently used to scrutinize the hypothesized sail-effect theory.

## 2. Reference frame definitions and terminology

Prior to presentation of the experimental apparatus and procedures in the subsequent section, we provide clarification of the relevant variables and coordinate systems. The provided definitions largely follow the work of Tew and Sayers (1999).

Fig. 1 (left) shows a cyclist moving at a velocity $V_{bg}$ relative to the ground. The direction of travel defines the main reference frame $\boldsymbol{X}_b$, pertaining to the bicycle, with the x-axis pointing opposite to the motion direction. In an external environment, the wind velocity $V_{ext}$ and its direction ($\gamma$, the crosswind angle) relative to the cyclist's direction of motion are relevant for the definition of the aerodynamic problem. The vector difference of external wind $\boldsymbol{V}_{ext}$ and bicycle ground velocity $\boldsymbol{V}_{bg}$ determines the relative wind velocity $\boldsymbol{V}_{rel}$ experienced by the cyclist. The angle between the cyclist's motion axis and the relative wind velocity defines the yaw angle $\beta$. Let us define a second coordinate system $\boldsymbol{X}_{wt}$ whose $x$-axis is aligned with $\boldsymbol{V}_{rel}$. The subscript '$wt$' signals that this reference frame pertains to the wind-tunnel when testing in a laboratory environment, where the $x$-axis is always aligned with the relative wind direction.

Fig. 1 (right) illustrates the resistive and lateral forces acting on a bicycle wheel. Classically, the drag force $D$ acts parallel to the free-stream direction defined by $\boldsymbol{V}_{rel}$, whereas the lift force $L$ points perpendicular to it, combining to the resultant force $\boldsymbol{F}_{tot}$. More relevant for a cyclist, however, are the force components in the reference frame $\boldsymbol{X}_b$ connected to the direction of motion. The side force $F_s$ and the axial force $F_a$ are expressed as geometrical projections of $L$ and $D$:

$$F_a = D\cos(\beta) - L\sin(\beta) \tag{1}$$

$$F_s = D\sin(\beta) + L\cos(\beta) \tag{2}$$

From equation (1), it follows that a situation may arise in which $L\sin(\beta) > D\cos(\beta)$, resulting in a negative axial force, that is a thrusting force which supports the cyclist's motion — the sail effect. In the remainder of this work, forces are always provided and discussed in the bicycle reference frame.

## 3. Experimental apparatus and procedures

Wind tunnel measurements are conducted at the TU Delft Open Jet Facility, an open jet, atmospheric wind tunnel with a $2.85 \times 2.85\ m^2$ exit section. All measurements are executed at a freestream velocity of 12.5 m/s (45 km/h). The turbulence intensity in the test section is reported with 0.5% by Lignarolo et al. (2014), which agrees well with freestream measurements conducted in the framework of the presented work. An overview of the test setup is provided in Fig. 2.

### 3.1. Wheel model & mechanical setup

A DT Swiss ARC 1100 Dicut DB 62 front wheel is installed in the test section. The 28" (700 mm diameter with tire fitted) wheel features a 62 mm deep and 27 mm wide carbon rim. While the wheel is designed to run with disc brakes, no brake discs were installed during the wind tunnel test. The clincher rim is fitted with a 25 mm tire, inflated at 7 bar. A Continental GP 5000 tire featuring a mild periodic surface pattern is chosen as a baseline tire, which is compared to a slick tire, a Continental GP TT. The slick tire is tested in two configurations:

1. The tire including a tripping element on the tread. The new tire features a production seam on the tread center. This seam is used to trigger boundary layer transition.
2. Subsequently, the seam is sanded down, resulting in a smooth tire tread.

For the baseline tire, the production seam is removed for all tests. The difference in tire profile is shown in Fig. 3. The grooved texture element on the baseline tire model is approximately 35 mm long, and 12 mm wide, with a 35 mm gap along the circumference between two subsequent elements.

The wheel is connected to the support structure using a $12 \times 100$ mm through axle. The single-sided support holding the wheel from the left hand side is designed to enhance optical access for the velocimetry measurements.

The tire rests on two 70 mm diameter (60 mm width) rollers embedded in the wooden ground plate. The rearward roller is driven by a variable speed DC motor to control wheel rotation. The wheel rotational speed is kept constant, matching a ground velocity ($V_{bg}$) of 12.5 m/s equal to the freestream velocity. Wheel rotational speed and free-stream velocity are both maintained constant at all times, and only the yaw angle is adjusted during the measurements. The wheel's rim is painted matt black to limit background reflections in the PIV acquisition. Based on the fact that no roughness could be perceived when

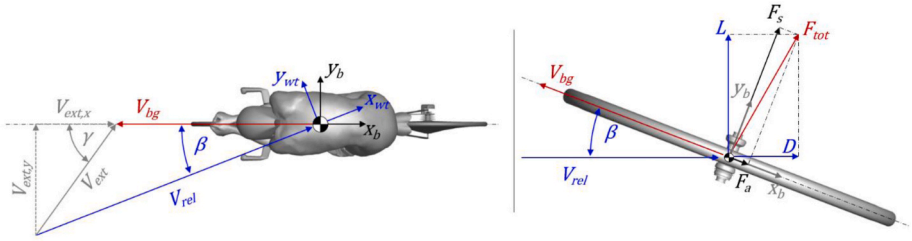


**Fig. 1.** Definition of axes systems, flow angles and velocities for a cyclist moving at a velocity $V_{bg}$ relative to the ground (left). Relation of forces in wind and bike reference frames, illustrated on a bicycle wheel in top view (right).

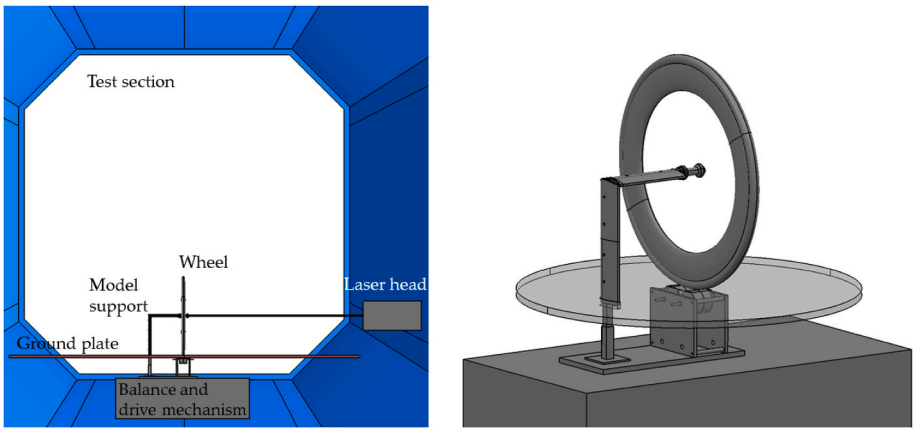


**Fig. 2.** Sketches of the experimental setup in the Open Jet Facility (left) and details of the model support and drive mechanism, with surrounding floor plates removed (right). The detailed CAD drawings are provided as supplementary material.

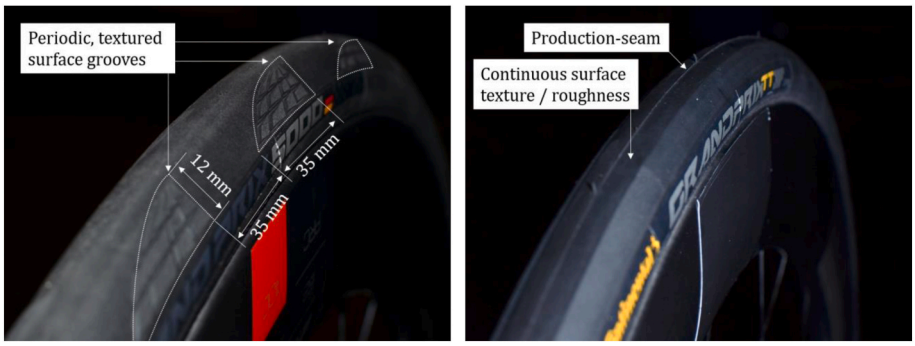


**Fig. 3.** Tested tires. (Left) Baseline tire, Continental GP 5000, with approximate indication of texture element size. (Right) Option tire, Continental GP TT.

touching the rim, it can be concluded that the application of the paint yields a smooth surface. Tire labels are equally covered by black ink.

### 3.2. Force measurement system

The wheel model including the mechanical support and drive mechanism is installed on a 6-axis force balance situated underneath the ground plate. The balance acquires data at a frequency of 2 kHz, and its accuracy is reported with 0.06% (0.15 N) and 0.23% (1.15 N) of its full load capacity, in the axial ($x$, $F_a$) and lateral ($y$, $F_s$) direction, respectively (Alons, 2008). Force data is acquired and averaged over 20 s. The balance is placed on a turntable that controls the yaw angle. As such, the force measurements delivered by the balance system pertain to the bicycle wheel reference frame ($\boldsymbol{X}_b$). The yaw angle $\beta$ is varied from $-24°$ to $+24°$ in steps of 2°. The arrangement of the components is illustrated in Fig. 2 (right). The vertical support (a NACA symmetric profile) is yawed with the rest of the setup. Due to the relatively large distance between the vertical support and the wheel (30 cm, or 0.86 wheel's radii), the interference effect between support and wheel is deemed negligible. As customary for bicycle wheel aerodynamic force measurements (see for instance Tew and Sayers, 1999), prior to force measurements on the wheel, the forces on the isolated support are recorded for all yaw angles of interest. This data is subsequently subtracted from the measurements with the wheel installed to identify the forces generated by the wheel only.

### 3.3. Particle image velocimetry system

Planar (2D-2C) PIV data is acquired in a horizontal plane at hub-height, imaging a 204 mm × 172 mm field of view. The images capture the most upstream section of the wheel, and the flow over the leeward side of tire and rim. The PIV camera, a LaVision sCMOS 16-bit camera with a 2560 × 2160 px$^2$ sensor and a 35 mm lens, is installed on the turntable, imaging the flow past the wheel through a Plexiglas window in the floor. Therefore, the camera is at all times aligned with the wheel's riding direction. A top view showing the relative position of wheel and camera is provided in Fig. 4.

At each yaw angle, 300 image pairs are acquired at a frequency of 15 Hz, with a time separation of 70 μs between two frames. Illumination is provided by a Quantel Evergreen 200 Nd:YAG laser (532 nm wavelength, 200 mJ maximum pulse energy). A Safex fog generator seeds the flow with water-based micron sized droplets of approximately 1 μm diameter.

Raw PIV images are pre-processed using an anisotropic diffusion filter (Adatrao and Sciacchitano, 2019), which effectively filters the continuous light reflection on tire and rim surface, as well as the occasional sharp reflection resulting from spokes passing the laser sheet. An example of a raw and processed image is provided in Fig. 5.

Image pairs are evaluated by a 3-pass cross-correlation with decreasing window size, reaching a final window size of 16 × 16 px$^2$. At 75% overlap the instantaneous velocity field features a vector spacing of 0.32 mm in both axes. Lastly, the velocity data is time averaged to yield the mean flow field and its statistical fluctuations. All processing steps are executed in the LaVision software Davis 10.2. The expanded uncertainty of the time-average velocity at 95% confidence level has been evaluated based on the local flow fluctuations and number of samples (Sciacchitano and Wieneke, 2016); its values range between 0.02 m/s in the potential flow region to 0.6 m/s in the separated region in the wheel's wake.

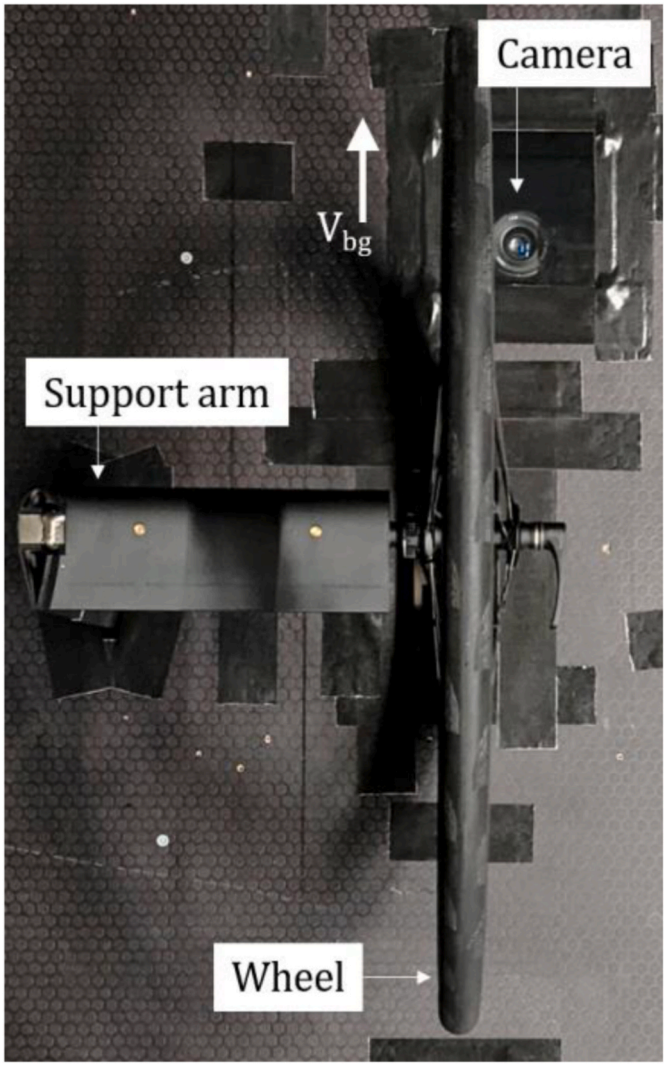


**Fig. 4.** Wheel in top-view with PIV camera visible through the Plexiglas window on the top right.

## 4. Results and discussion

The analysis of the measurement data starts with the force measurements. Subsequently, the velocimetry data is analyzed, and the practical relevance of the presented results is discussed.

### 4.1. Force measurement

Fig. 6 displays the force measurements versus yaw angle in the bicycle reference frame for the three tested tire options.

For moderate yaw angles within $|\beta| \leq 8^\circ$ the recorded forces are equivalent for all tested tires. In this range, the lateral force reduces by approximately 0.85 N/°. The angle of zero side force is slightly negative at about $-0.8^\circ$, which is mainly attributed to the uncertainty of the yaw angle estimation (about 0.5°) and the presence of the support which alters the symmetry of the flow in straight ahead conditions, giving rise to a non-zero lateral force.

For yaw angles exceeding 8° magnitude, the linear behavior in the lateral force is only continued for the smooth tire with the production seam, i.e. the tire with the tripping element. For this wheel-tire combination, the linear behavior continues until 16° yaw, where the slope tapers off. For the tires without the production seam, the lateral force magnitude increases at a significantly reduced rate for yaw angles in excess of 8°.

The differences observed in the lateral force translate also into the axial force readings. For moderate yaw angles within 8°, the tires behave similarly, showing maximum resistance at (near) zero yaw angle. For small non-zero yaw angles the aerodynamic resistance decreases. For yaw angles in excess of 8°, the resistive force keeps decreasing only for the slick tire with the production seem, i.e. the tire with the tripping element. The smallest resistive force for this tire is recorded at 16° yaw, where a negative resistance of $-0.05$ N is measured. Beyond 16°, a steep increase in axial resistance is observed. Such increase in axial force, along with a stagnating lateral force, is signifying that the flow over the wheel is separated, which is confirmed later by the velocimetry data in Sec. 4.2.

If the production seam is removed from the slick tire, the axial force reduction stops already at 8°, indicating that flow separation occurs as much as 8° earlier when comparing to the tire with the tripping element. The textured tire behaves similar to the slick tire. Only for negative yaw angles the increase in resistive force is observed below $-12^\circ$ for the textured tire, as compared to $-8^\circ$ for the slick tire.

The wind-averaged drag (Ingram, 1978) is evaluated considering a cycling speed of 12.5 m/s and a wind speed of 3 m/s, similar to Brownlie et al. (2010). The wind-averaged drag values are 0.96 N, 0.67 N and 1.11 N for the GP 5000 (textured), GP TT (with seam) and GP TT (smooth) tires, respectively. Hence, although the higher yaw angles have lower influence on the wind-averaged drag, clear differences among the different tires are noticed.

The above force data confirms the sail-effect hypothesis: at high yaw angles, the wheel is able to generate a thrusting force, albeit small in magnitude. Importantly, the extent of the resistance reduction is observed to be strongly dependent on the tire surface characteristics. For a better understanding of the tire dependence, the velocimetry data is compared in the following.

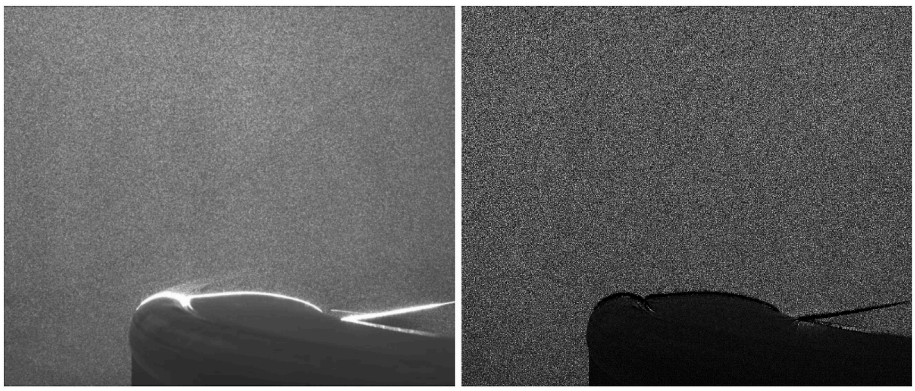

**Fig. 5.** Example of raw (left) and pre-processed (right) image.

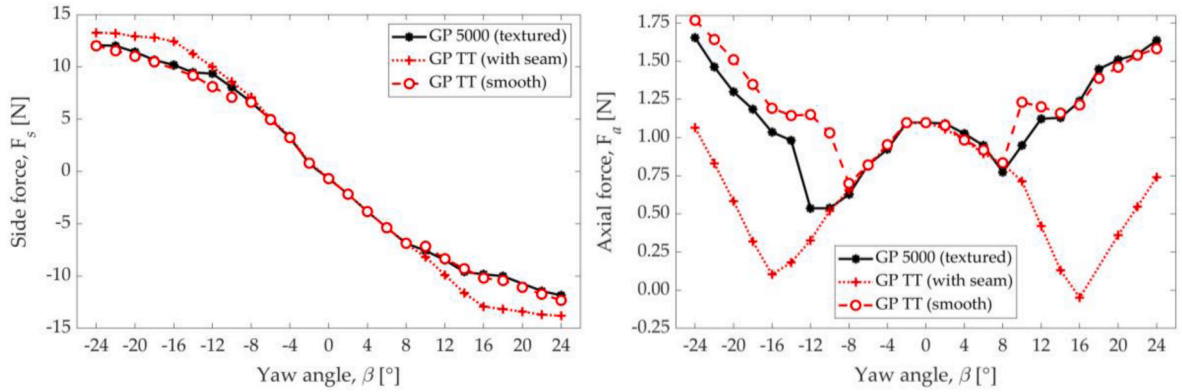


**Fig. 6.** Force measurements on the isolated wheel for different tire options. (Left) lateral force. (Right) resistive force.

### 4.2. Velocimetry data

The PIV data is collected at hub-height, on the leeward side of the most upstream section of the wheel. Velocities are plotted in the bicycle wheel reference frame, such that $u$ points opposite to the riding direction. Fig. 7 shows normalized velocity contours of $u^*$ for the three tested tire options for increasing yaw angles. Velocity normalization is based on the axial freestream velocity component ($u_{wt_0} \cdot \cos(\beta)$), i.e. the component of the freestream aligned with the riding direction. Additionally, in-plane streamlines are plotted to provide information on the lateral velocity component.

At 0° yaw the three tire options behave equivalently: the flow stagnates on the tread center, followed by an acceleration on the side of the tire and the rim. The region of accelerated flow is characterized by two local maxima of the velocity: one on the side of the tire and a second one near the thickest point of the rim. Thus, a local region of adverse pressure gradient must be anticipated close to the tire-rim junction. Downstream of the rim, a region of reverse flow is observed.

At 8° yaw, the three tire options still behave similarly. The stagnation point has rotated towards the windward side. The region of accelerated flow is larger and more intense. Compared to straight ahead conditions with two local velocity maxima, only one region of maximum velocity is visible, which is located near the tire-rim junction. The recirculating flow in the rim's wake is slightly more pronounced, and similar to the other features is rotated counter-clockwise as compared to the 0° case.

The first substantial difference between the tires is observed at 12° yaw, where the flow past the wheel with the smooth tire is fully separated, compared to the same tire with the tripping element where the flow is mostly attached. The flow over the wheel with the textured tire is also separated; the separation zone is, however, smaller when compared to the fully smooth tire.

Considering the velocity fluctuations ($u'_{rms}$) for 12° yaw angle shown in Fig. 8, one finds that the velocity variation near the rim-tire junction is stronger and distributed over a larger area for the textured tire, as compared to the smooth tire which features a confined region of peak velocity fluctuation near the widest section of the tire. This suggests that the smooth tire features a well-defined flow separation point, whereas the textured tire features a varying point of separation that oscillates approximately between the widest points of rim and tire. The smooth tire with the tripping element on its tread shows an elongated zone of high velocity fluctuations in vicinity of the rim, suggesting the presence of a thick, turbulent boundary layer.

The variation in the separation point location is highlighted by analyzing the probability of positive streamwise flow velocity near the tire-rim profile as function of the streamwise coordinate in Fig. 9. For the smooth tire, the probability of forward flow over the profile drops sharply just ahead of the tire-rim junction, near x/c = 0.2, indicative for a fixed separation point at this location. In contrast, the smooth tire with the production seam maintains a probability of positive streamwise flow velocity in excess of 90% until x/c = 0.8, confirming that with the tripping element on the tire the flow remains mostly attached. The data for the periodically textured baseline tire falls in between these two cases: the probability of forward flow velocity drops significantly near x/c = 0.25; however, it remains above 33% until x/c = 0.6, signaling that for more than one third of the measurements the flow remains attached over this section of the tire-rim profile, and flow separation is delayed.

Based on the above observations, it is concluded that,

1. The production seam on the smooth tire does indeed trigger the laminar-to-turbulent boundary layer transition. The turbulent boundary layer remains attached to the rim-tire profile.
2. Without the production seam, the smooth tire features a laminar boundary layer, that separates from the tire at its widest section.
3. The grooved elements on the textured tire yield an oscillating separation point. It is therefore speculated that the roughness elements on the textured tire, similar to the tripping element on the smooth tire, trigger local boundary layer transition and thereby, push the flow separation point further downstream. Between the periodic roughness elements the tire behaves similar to the smooth tire, featuring a "leading-edge" separation.

The difference between the flow states on the textured tire is highlighted by conditionally averaging the flow field, based on the size of the (instantaneous) zone of recirculating flow in the measurement plane, i.e. the number of velocity vectors reading a negative streamwise velocity component. Isolating and averaging 10% (30 vector fields, each) of the measurements with the smallest (respectively, the largest) zone of recirculation yields the velocity contours shown in Fig. 10. These conditional averages show that, for this tire and yaw angle, the flow varies between a mostly attached state (Fig. 10 - left) and a fully separated state (Fig. 10 - right). The flow states cannot be linked to the relative position of the roughness elements on the tire with respect to the measurement plane, for the available data. Provided that this behavior is only observed on the periodically textured baseline tire, however, supports the hypothesis that the grooved elements on the tire surface drive the observed variation in the flow separation.

Overall, for 12° yaw angle, the observed flow fields correlate well with the force data in Sec. 4.1, where at 12° it was found that the smooth tire with tripping element features by far the lowest resistance, followed by the textured tire, and lastly the fully smooth option.

At 16° yaw, the smooth and textured tire behave equivalently, with both options featuring a large zone of recirculating flow, starting upstream of the tire-rim-junction. The $u'_{rms}$ contours for the two tires in Fig. 8 are now also similar, indicating that both tires feature a well-defined flow separation point. The smooth tire with tripping element,

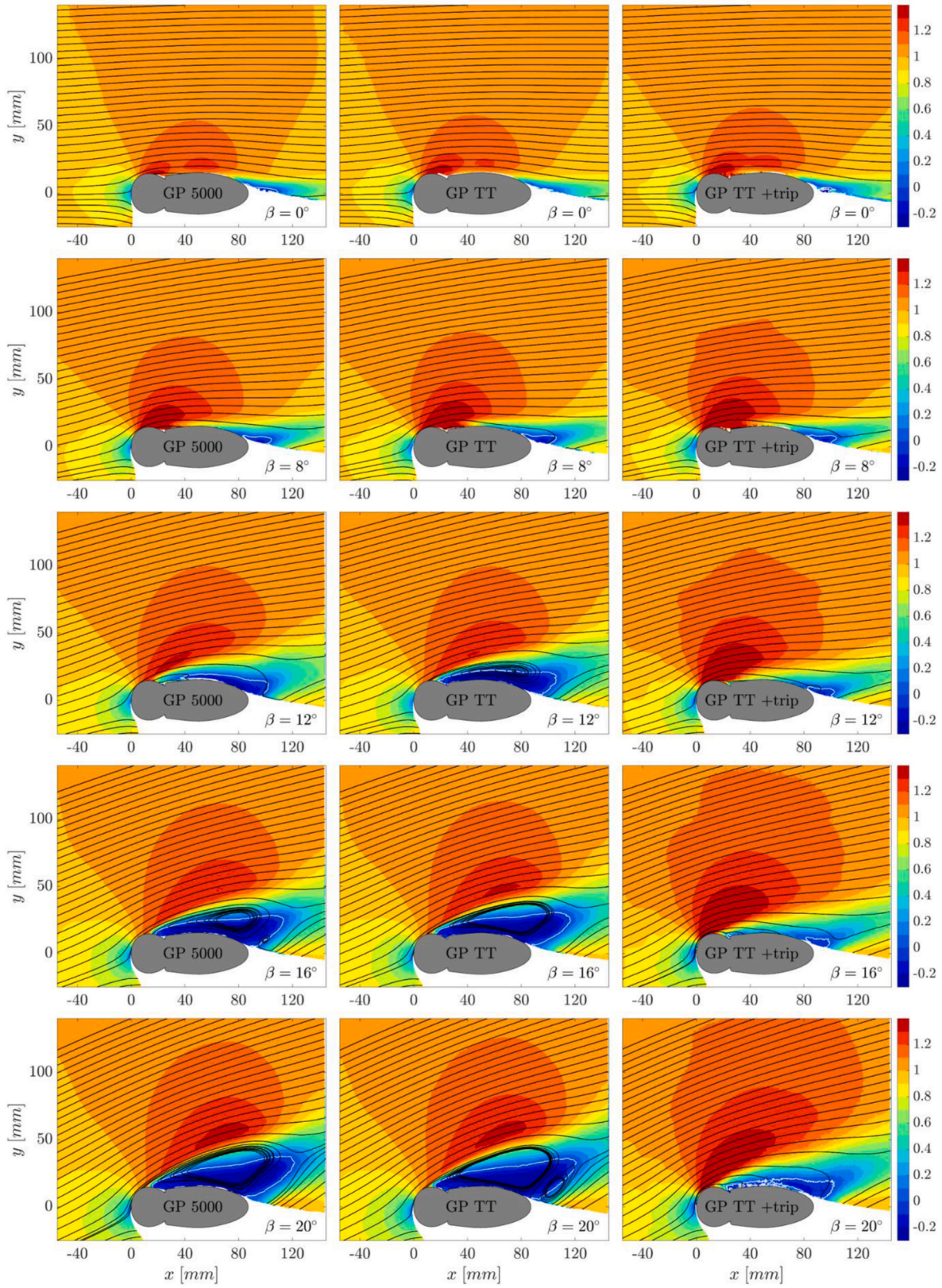


**Fig. 7.** Mean u*-velocity contours for increasing yaw angle. Zero-velocity contour highlighted in white. Left column showing wheel with baseline tire, center column pertains to the slick tire, and the right column presents the slick tire including the boundary-layer tripping element.

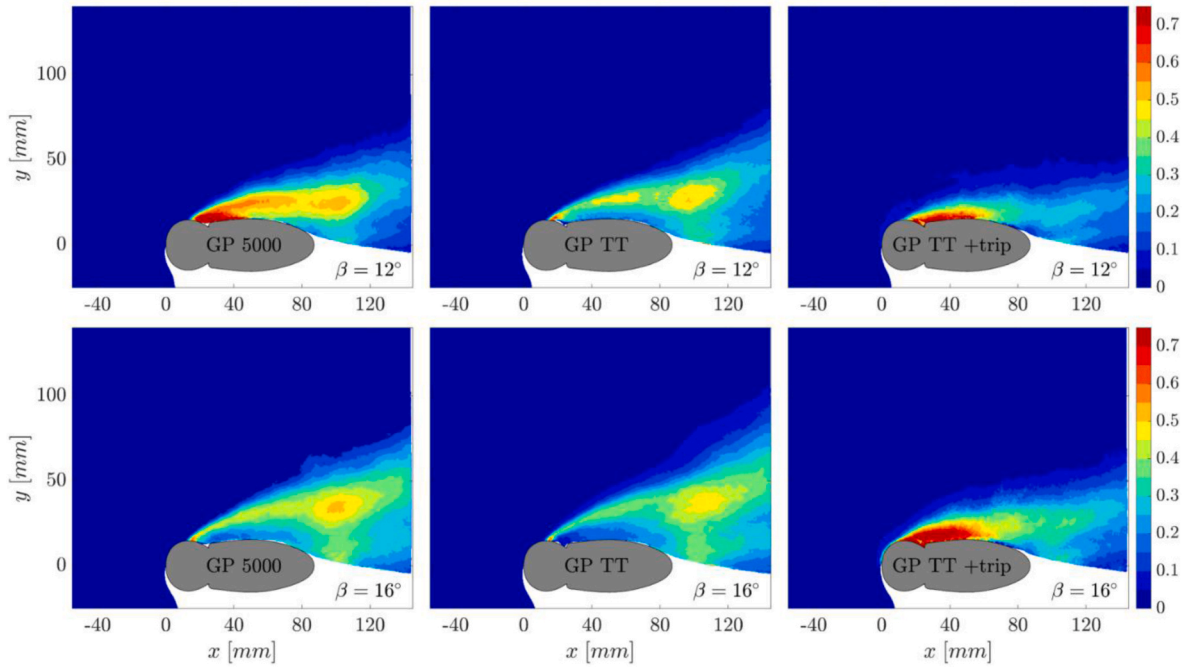


**Fig. 8.** Statistical velocity fluctuations $u'_{rms}$ at 12° and 16° yaw. Contours normalized by the axial freestream velocity component.

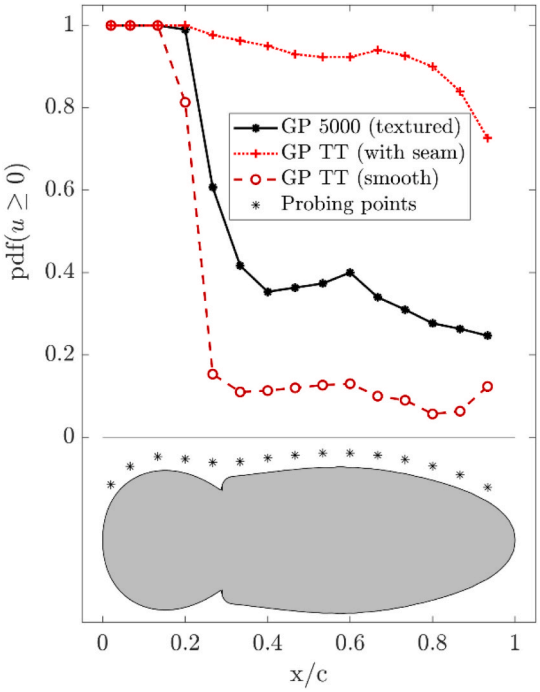


**Fig. 9.** Probability of positive streamwise velocity near the tire-rim section as function of streamwise distance x/c for the three tested tires at 12° yaw. Probing point locations indicated by black stars.

instead, features an attached flow over the tire and rim.

At the largest considered yaw angle of 20° all three tire options show a clear flow separation. The separated zone on the smooth tire with tripping element is still significantly smaller compared to the other two options.

### 4.3. Practical implications

The force- and velocimetry-data analysis has proven that the tire surface structure is an important design parameter when attempting to minimize the aerodynamic drag of a road bicycle wheel. The production seam on the tread of the smooth tire worked as an effective element to trigger laminar-to-turbulent boundary layer transition. The latter is found to be essential for maintaining attached flow over the tire-rim section at yaw angles exceeding 8°.

It is clear that the production seam cannot function as a boundary layer tripping device in real cycling conditions, given that it rapidly wears off when ridden on tarmac under a rider's load. On the opposite side, when studying bicycle wheel performance through computational fluid dynamic (CFD) simulations, appropriate modelling of the tire characteristics is essential for obtaining realistic flow topology and load estimates. In the wind-tunnel environment it is shown that the potential gain that can be realized when tripping the boundary layer on the tire is large: the stall angle is increased by as much as 8°, reducing the wind averaged drag (Barry, 2018) by 33% when considering a mean wind-speed of 3 m/s that follows a Weibull distribution ($k = 2$) at a riding velocity of 12.5 m/s. The texture of the baseline tire still yields an 8% drag reduction relative to the fully smooth tire.

The flow topology comparison of smooth and textured tire at moderate yaw angle (12°) indicates that the grooved elements on the textured tire bear the potential of delaying flow separation locally. Optimization of the texture elements for aerodynamic performance is therefore deemed to be essential, and should be considered by both, tire and wheel manufacturers. Likewise, reporting force measurements on a road bicycle wheel is only meaningful if the tire specifications are also provided.

## 5. Conclusion

The aerodynamic characteristic of a state-of-the-art road cycling wheel in cross wind has been assessed experimentally by means of force and PIV measurements. Specific attention is paid to the interaction of rim and tire, by comparing the wheel's behavior with changing tire surface texture. The resistive force on the isolated wheel is highest in

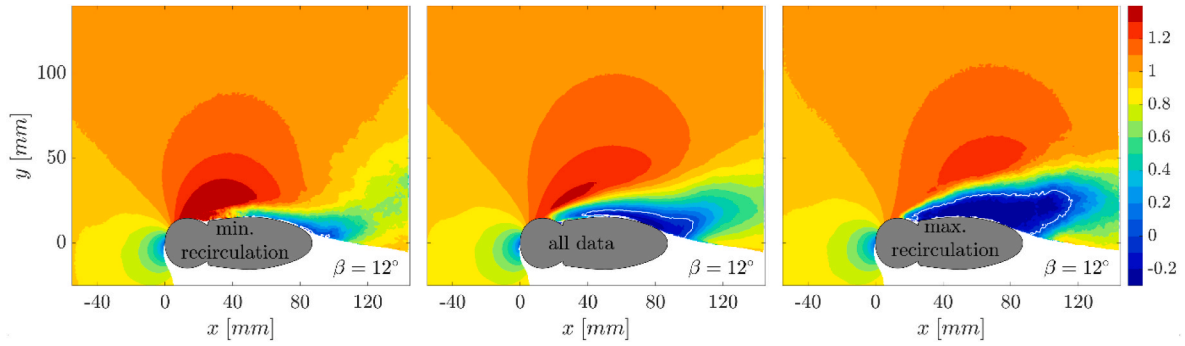


**Fig. 10.** Conditionally averaged u*-velocity contours for 12° yaw angle on the wheel with the baseline tire. Zero-velocity contour highlighted in white. Data on the left computed from 30 instantaneous flow fields (10%) containing smallest area of flow reversal; center shows average of full dataset; right contour computed from 30 instantaneous flow fields containing largest region of recirculation.

straight ahead conditions ($\beta = 0°$). The aerodynamic resistance of the wheel is reduced as the yaw angle magnitude increases. Analysis of the velocimetry data confirms that the reduction in resistance measured by the force balance is indeed a consequence of the sail-effect, resulting from a substantial side-force on the wheel at yaw incidence. The benefit of this effect is limited by the stall angle of the tire-rim combination, which is found to depend significantly on the tire choice. A greater stall angle is obtained if the tire triggers laminar-to-turbulent boundary layer transition. For the tested tires differences of up to 8° in stall angle are obtained, that ultimately result in a 33% difference in wind-averaged drag for the tested 62 mm deep wheel.

## CRediT authorship contribution statement

**Constantin Jux:** Conceptualization, Data curation, Investigation, Methodology, Software, Visualization, Writing – original draft. **Andrea Sciacchitano:** Conceptualization, Supervision, Writing – review & editing. **Fulvio Scarano:** Conceptualization, Supervision, Writing – review & editing.

## Declaration of competing interest

The authors declare that they have no known competing financial interests or personal relationships that could have appeared to influence the work reported in this paper.

## Data availability

Data will be made available on request.

## Appendix A. Supplementary data

Supplementary data to this article can be found online at https://doi.org/10.1016/j.jweia.2022.105294.

## References

Adatrao, S., Sciacchitano, A., 2019. Elimination of unsteady background reflections in PIV images by anisotropic diffusion. Meas. Sci. Technol. 30 https://doi.org/10.1088/1361-6501/aafca9.

Alons, H.J., 2008. OJF External Balance. Nationaal Lucht en Ruimtevaartlaboritorium (National Aerospace Laboratory; NLR), NLR-CR-2008-695.

Barry, N., 2018. A new method for analysing the effect of environmental wind on real world aerodynamic performance in cycling. In: 12th Conference of the International Sports Engineering Association. https://doi.org/10.3390/proceedings2060211.

Barry, N., Burton, D., Crouch, T., Sheridan, J., Luescher, R., 2012. Effect of crosswinds and wheel selection on the aerodynamic behavior of a cyclist. In: Engineering of Sport Conference 2012. https://doi.org/10.1016/j.proeng.2012.04.005.

Brownlie, L., Ostafichuk, P., Tews, E., Muller, H., Briggs, E., Franks, K., 2010. The wind-averaged aerodynamic drag of competitive time trial cycling helmets. Procedia Eng. 2, 2419–2424. https://doi.org/10.1016/j.proeng.2010.04.009.

Cant, G., 2014. Back to the wind tunnel. https://www.swissside.com/blogs/news/back-to-the-wind-tunnel. (Accessed 17 May 2021). Accessed.

Cooper, K.R., 2003. Truck aerodynamics reborn-lessons from the past. SAE Trans. 112, 132–142.

Crane, R., Morton, C., 2018. Drag and side force analysis on bicycle wheel-tire combinations. J. Fluid Eng.-T ASME 140. https://doi.org/10.1115/1.4039513.

Godo, M., Corson, D., Legensky, S., 2010. A comparative aerodynamic study of commercial bicycle wheels using CFD. In: 48th AIAA Aerospace Sciences Meeting Including the New Horizons Forum and Aerospace Exposition.

Greenwell, D.I., Wood, N.J., Bridge, E.K.L., Addy, R.J., 1995. Aerodynamic characteristics of low-drag bicycle wheels. Aeronaut. J. 99, 109–120. https://doi.org/10.1017/S0001924000028281.

Ingram, K.C., 1978. The wind-averaged drag coefficient applied to heavy goods vehicles. In: Australian Road Research Board Symposium. No. Supp. Report 392).

Kyle, C.R., Burke, E., 1984. Improving the racing bicycle. Mech. Eng. 106, 34–45.

Lignarolo, L.E.M., Ragni, D., Krishnaswami, C., Chen, Q., Ferreira, C.J.S., van Bussel, G.J. W., 2014. Experimental analysis of the wake of a horizontal-axis wind-turbine model. Renew. Energy 70, 31–46. https://doi.org/10.1016/j.renene.2014.01.020.

Lukes, R.A., Chin, S.B., Haake, S.J., 2005. The understanding and development of cycling aerodynamics. Sports Eng. 8, 59–74. https://doi.org/10.1007/BF02844004.

Malizia, F., Blocken, B., 2020a. Bicycle aerodynamics: history, state-of-the-art and future perspectives. J. Wind Eng. Ind. Aerod. 200 https://doi.org/10.1016/j.jweia.2020.104134.

Malizia, F., Blocken, B., 2020b. CFD simulations of an isolated cycling spoked wheel: the impact of wheel/ground contact modeling in crosswind conditions. Eur. J. Mech. B Fluid 84, 487–495. https://doi.org/10.1016/j.euromechflu.2020.07.009.

Malizia, F., Montazeri, H., Blocken, B., 2019. CFD simulations of spoked wheel aerodynamics in cycling: impact of computational parameters. J. Wind Eng. Ind. Aerod. 194 https://doi.org/10.1016/j.jweia.2019.103988.

Sciacchitano, A., Wieneke, B., 2016. PIV uncertainty propagation. Meas. Sci. Technol. 27 (8), 084006 https://doi.org/10.1088/0957-0233/27/8/084006.

Tew, G.S., Sayers, A.T., 1999. Aerodynamics of yawed racing cycle wheels. J. Wind Eng. Ind. Aerod. 82, 209–222. https://doi.org/10.1016/S0167-6105(99)00034-3.

Zdravkovich, M., 1992. Aerodynamics of bicycle wheel and frame. J. Wind Eng. Ind. Aerod. 40, 55–70. https://doi.org/10.1016/0167-6105(92)90520-K.